

# Rock Mass Deformation Characteristics in High-Steep Slopes Influenced by Open-Pit to Underground Mining

Chuanbo Zhou · Shiwei Lu · Nan Jiang ·  
Dingbang Zhang · Zhihua Zhang · Gaojian Miao

Received: 15 April 2015 / Accepted: 4 April 2016 / Published online: 8 April 2016  
© Springer International Publishing Switzerland 2016

**Abstract** In Daye Iron Mine, the open-pit mining has ended and the underground mining started in 2003. The present pit slopes are as high as 430 m and the slope angle is up to 43°. During the process of open-pit to underground mining, the high-steep pit slopes would be affected by both open-pit mining and underground mining, and its deformation characteristics would become more complex. So in this paper, the trinity method of numerical simulation, model experiment and field test was adopted to analyze the displacement and stress fields systematically. The results show that: (1) Prominent rebound deformation occurs near the slope foot, which is induced by the unloading in open-pit mining. When it is backfilled to 0 m level, the rebound deformation decreases, which indicate that backfilling mass can restrict the deformation and improve the slope stability; (2) Subsidence dominates the slope deformation in open-pit to underground mining and it increases with an increasing elevation of monitoring point; the maximum horizontal displacement occurs in the lower part of the slopes, because the backfilled part is squeezed by both the north slope and the south slope, and it has a lower elastic modulus than the previous orebody; (3) The stress and its variability near the slope foot are

much larger than other places, indicating that the slope foot is most affected by stress redistribution and stress concentration may occur here; the stress at other stress monitoring points changes little, indicating that the influence of open-pit to underground mining is local; (4) The effect of underground mining on the deformation of the faults is not prominent; (5) Mining operations in near-ground part affect more on the variation of deformation and stress of pit slopes than that in deeper part.

**Keywords** Open-pit to underground · High-steep slope · Deformation characteristics · Numerical simulation · Model test

## 1 Introduction

With shallow resources exhausting around the world, high-steep slopes, formed by open-pit mining, threaten the mine safety production. To ensure the stability of high-steep slopes influenced by open-pit to underground mining, analysis of deformation characteristics has an important theoretical and practical value.

Recent research on the stability of high-steep pit slopes influenced by underground mining have been carried out by using many methods, such as theoretical analysis, numerical simulation and model test. The stability of high slopes was evaluated based on the limit equilibrium method (Huang et al. 2012; Tan et al.

---

C. Zhou · S. Lu · N. Jiang (✉) · D. Zhang ·  
Z. Zhang · G. Miao  
Faculty of Engineering, China University of Geosciences,  
No. 388, Lumo Road, Wuhan 430074, Hubei, China  
e-mail: happyjohn@foxmail.com

2013), block theory (Kulatilake et al. 2011), fuzzy mathematics theory (Daftaribesheli et al. 2011), neural network theory (Kaunda et al. 2010) and so on; Numerical simulation methods, such as Finite Element Method (FEM) (Chen et al. 2001; Yao et al. 1993), Numerical Manifold Method (NMM) (He et al. 2013), Finite Difference Method (FDM) (Guo et al. 2013), discontinuous deformation analysis (DDA) (Ma et al. 2013), were more and more used to study slope stability and its deformation and failure; because model test can complement the deficiency of numerical simulation in the strata movement induced by mining, it has been used to study high-slope deformation and its failure (Chen et al. 2011). Meanwhile, few achievements have been published about slope stability influenced by open-pit to underground mining.

Based on the engineering practice of Daye Iron Mine, the FDM software FLAC<sup>3D</sup> was firstly used to study the deformation characteristics in high-step slopes induced by open-pit to underground mining. Then a physical model was also established to analyze the deformation on a certain cross-section plane to prove and complement the numerically simulated results. Finally, a field test was carried out to prove the reliability of conclusions.

## 2 General Information of the Project Site

Daye Iron Mine is located in Tieshan District, Huangshi City, Hubei Province, PR China, about 90 km west to Wuhan, 25 km east to Huangshi City, 15 km southeast to Daye. A deep open pit has been formed, measuring 2400 m long by 1000 m wide. The eastern part of the open-pit exploitation site was chosen as the study area, as shown in Fig. 1. The north slope is higher than the south slope. The height of the slopes varies between 130 and 430 m, and the slope angle varies between 38° and 43°. Marble mainly distributes in the south slope, diorite mainly distributes in the north slope, and magnetite mainly distributes in the contact zone. Alteration phenomenon can be observed nearby the contact zone, many sets of fracture structures exist in the study area, but only Fault F9 and Fault F25 have a great effect on the slope stability; the in situ stress test results indicate that no great tectonic stress appears.

## 3 Numerical Simulation and Results

### 3.1 Numerical Model and Calculation Conditions

In this paper, a three-dimensional model of Daye Iron Mine in the original geometry is established using the software FLAC<sup>3D</sup>, as shown in Fig. 2. It is measuring 900 m in *x*-direction by 800 m in *y*-direction by 680 m in *z*-direction. The model is transformed into a mesh of tetrahedron-shaped elements. The model mesh has 76,331 elements and 131,016 nodes. The surfaces around the model are applied for horizontal displacement constraints. The bottom surface is applied for fixed constraint. The top surface is free.

The accuracy of parameters is critical to the calculation results. Mohr–Coulomb (M–C) model is considered as the material model for numerical simulation (Cundall 1993). Based on laboratory tests (such as uniaxial compressive test, Brazilian test and shear test), the mechanical parameters of all materials are determined and listed in Table 1 (Zhang 2012).

### 3.2 Mining Scheme

The selection of a mining scheme significantly affects the stress field and the stability of slopes in a mine. In order to obtain the variation of the stress and the deformation matching reality as much as possible, the mining scheme was made according to the actual mining process. The mining steps are given in the following:

- Step 1* exploit down to –48 m level;
- Step 2* backfill to 0 m level with gravels;
- Step 3* exploit from –48 m down to –60 m level, then backfill the excavated part;
- Step 4* exploit from –60 m down to –72 m level, then backfill the excavated part;
- Step 5* exploit from –72 m down to –84 m level, then backfill the excavated part;
- Step 6* exploit from –84 m down to –96 m level, then backfill the excavated part;
- Step 7* exploit from –96 m down to –108 m level, then backfill the excavated part;
- Step 8* exploit from –108 m down to –120 m level, then backfill the excavated part;
- Step 9* exploit from –120 m down to –132 m level, then backfill the excavated part;

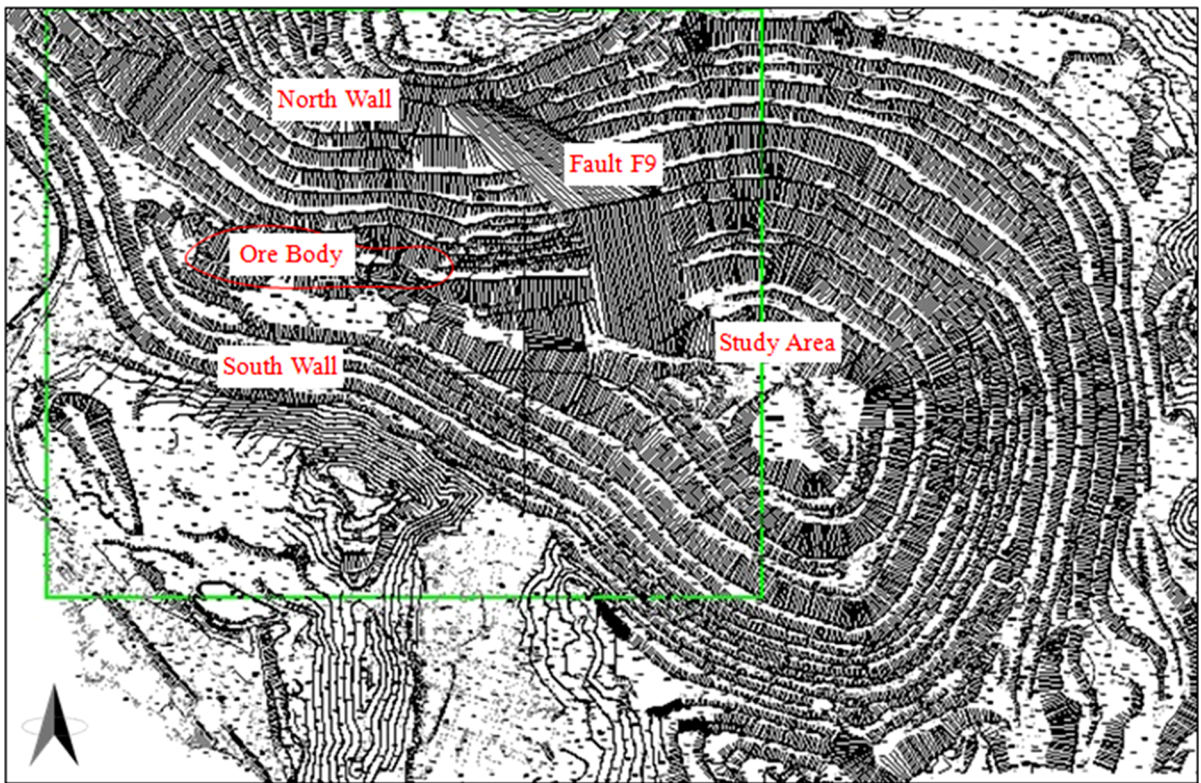


**Fig. 1** Study area (inside the green rectangle)

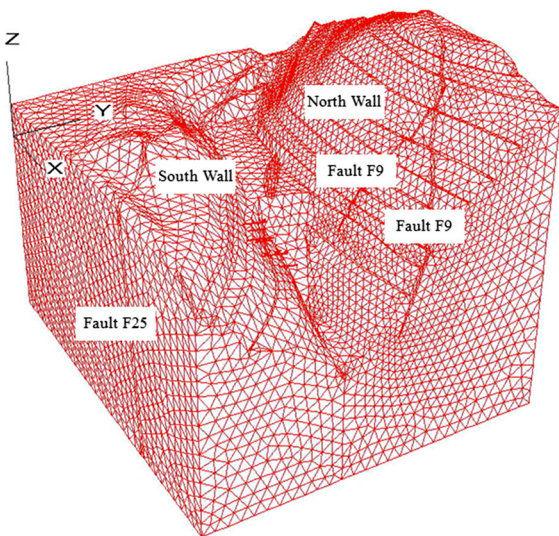


**Fig. 2** Finite difference grid and geometry of model

- Step 10* exploit from  $-132$  m down to  $-144$  m level, then backfill the excavated part;
- Step 11* exploit from  $-144$  m down to  $-156$  m level, then backfill the excavated part;
- Step 12* exploit from  $-156$  m down to  $-168$  m level, then backfill the excavated part;
- Step 13* exploit from  $-168$  m down to  $-180$  m level, then backfill the excavated part;

### 3.3 Results and Discussion

Three sets of displacement monitoring points are set on the sections  $x = 400$ ,  $x = 600$  and  $x = 700$  respectively, as shown in Fig. 3. The distances between the sections and the orebody increase successively, and the response characteristics of different parts of the entire slope influenced by open-

**Table 1** Rock properties in different zones of the model

Name	Young’s modulus E(GPa)	Poisson ratio	Cohesion (MPa)	Frictional angle (°)	Tensile strength (MPa)
Marble	15.6	0.23	0.254	28	0.25
Diorite	16.9	0.23	0.261	30	0.10
Magnetite	12.5	0.27	0.337	40	0.35
Backfilling material	2.0	0.20	0.070	27	0.02
Fault	1.7	0.20	0.128	23	0.04

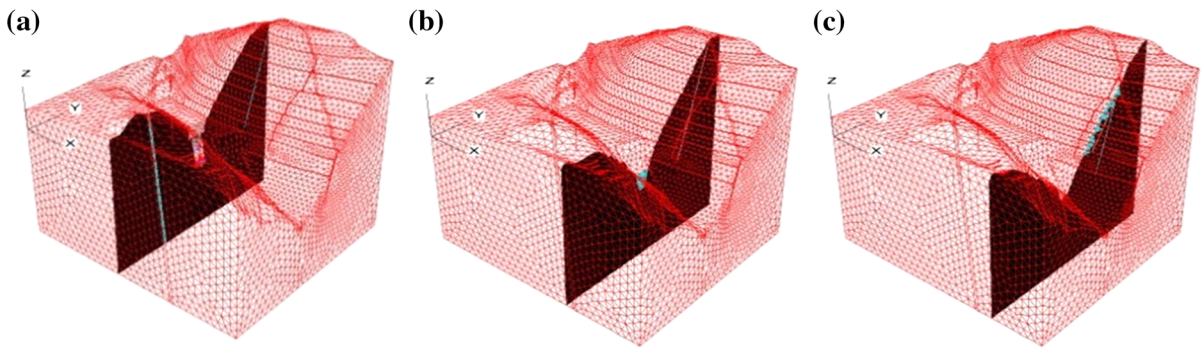


**Fig. 3** Locations of typical cross-section planes. **a**  $x = 400$ , **b**  $x = 600$ , **c**  $x = 700$

pit to underground mining can be obtained quantitatively.

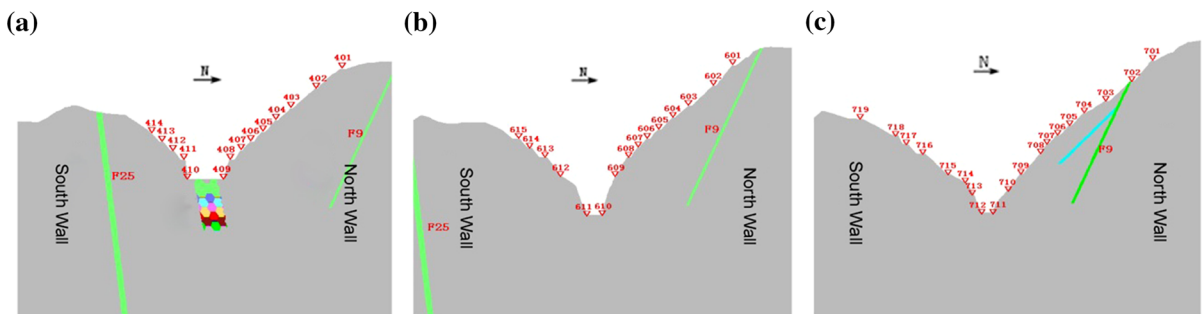
3.3.1 Deformation Analysis

Field displacement monitoring points are placed on the slope surface. In order to compare numerical simulations with physical reality, the displacement monitoring points in numerical simulation are set on the crest of each bench. 14, 15 and 19 displacement monitoring points are set on section  $x = 400$ ,  $x = 600$

and  $x = 700$  respectively. Displacement monitoring points on each cross-section plane were shown in Fig. 4.

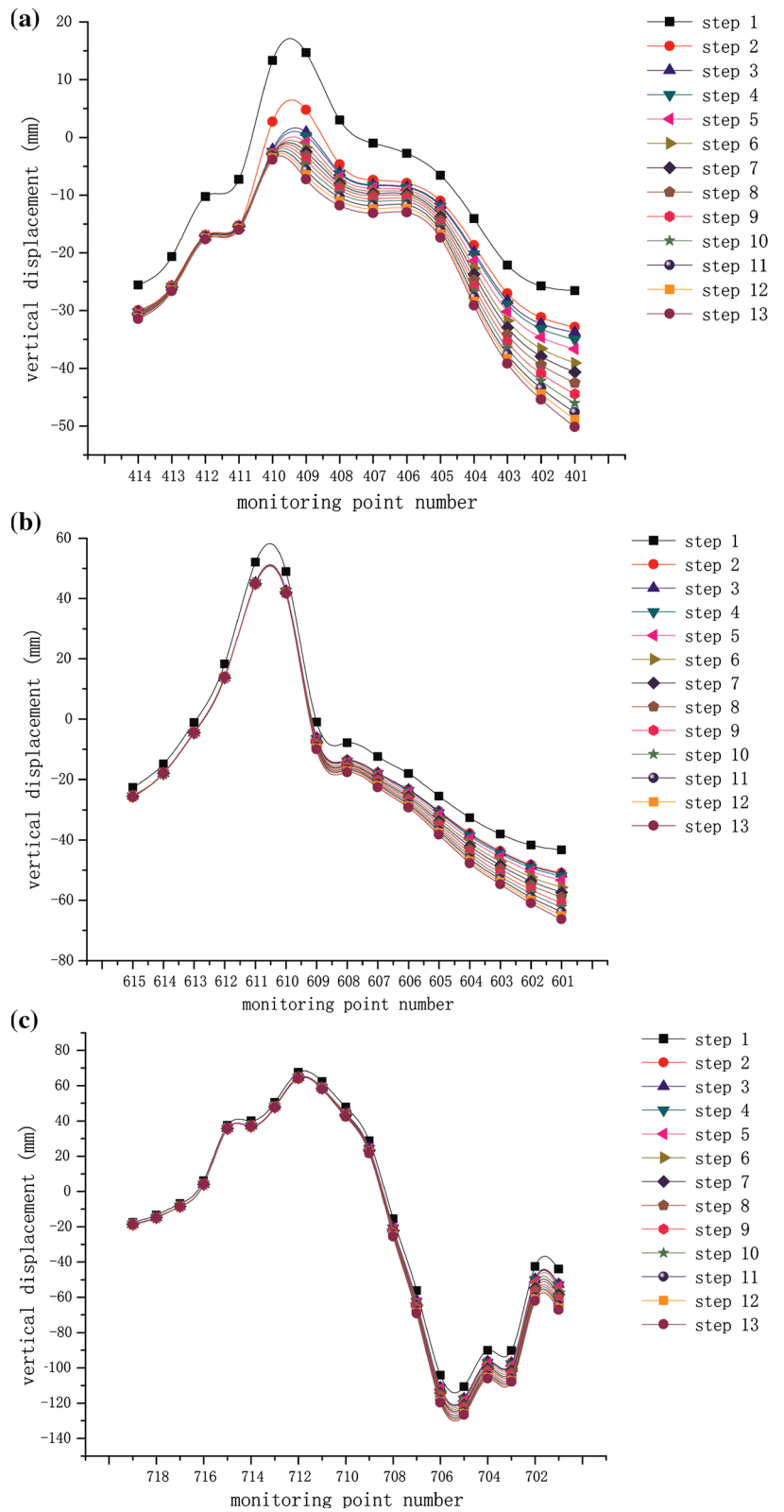
1. Vertical displacement

Figure 5 shows the total subsidence at displacement monitoring points on different sections when mining down to different levels. The difference between two different curves means the vertical displacement increment. The following observations are made:



**Fig. 4** Displacement monitoring points. **a**  $x = 400$ , **b**  $x = 600$ , **c**  $x = 700$

**Fig. 5** Subsidence curves at displacement monitoring points. **a**  $x = 400$ , **b**  $x = 600$ , **c**  $x = 700$



1. The shape and variation tendency of vertical displacement curves on different sections are similar, which implicates that the variation pattern of vertical displacement of the slopes in this paper induced by mining excavation is general.
  2. The vertical displacements decrease with an increasing horizontal distance between the monitoring section and the orebody, which implicates the influence of mining excavation decays with an increasing horizontal distance away from the mining area.
  3. In a single section, the maximum positive vertical displacement occurs at the slope foot when mining down to  $-48$  m, because a rebound phenomenon under unloading will be triggered by the excavated part, which is right at the slope foot.
  4. The largest vertical displacement increment occurs between step 1 and step 2, which implicates that the backfilled gravels at the slope foot can obviously restrain the vertical deformation.
  5. After backfilling to 0 m in step 2, the vertical displacement increment suddenly decreases, which means underground mining has a less influence on the vertical deformation than open-pit mining. In open-pit to underground mining, subsidence dominates the vertical deformation of slope. And when mining from  $-48$  to  $-96$  m, the vertical displacement increment between mining steps increases. After that, it decreases to its minimum when exploiting down to  $-168$  m level. This means underground mining in near ground area (before the  $-96$  m level) affects the vertical deformation of pit slopes more than that in deeper area (after the  $-96$  m level).
  6. In open-pit to underground mining, subsidence of the south slope is much less than that of the north slope because the north slope is much higher than the south slope, which implicates that the influence of open-pit to underground mining on a slope is proportional to the slope height. So the north slope is more likely to destabilize.
2. Horizontal displacement
 

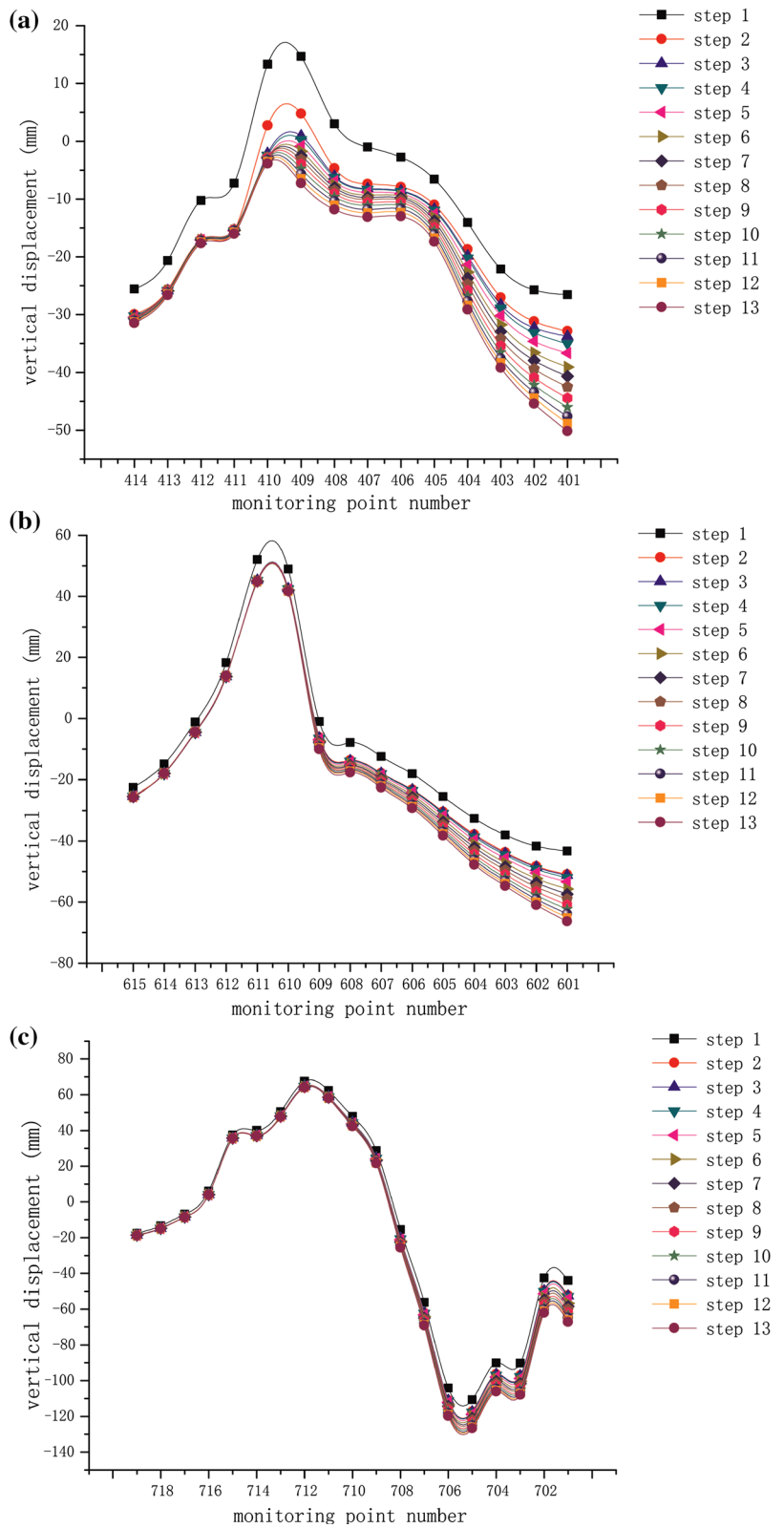
Figure 6 shows the total horizontal deformation at displacement monitoring points on different sections when mining down to different levels. The vertical distance between two different curves means the displacement variation. The following observations are made:

    1. The shape and variation pattern tendency of horizontal displacement curves on different sections are similar, which implicates that the variation pattern of horizontal displacement of the slopes in this paper induced by mining excavation is general.
    2. The horizontal displacements also decrease with an increasing horizontal distance between the monitoring section and the orebody, which implicates the influence of mining excavation on the horizontal deformation of slope decays with an increasing horizontal distance away from the mining area.
    3. Taken as a whole, in a single section, the largest horizontal displacement increment occurs between step 1 and step 2, which implicates that the backfilled gravels at the slope foot can obviously restrain the horizontal deformation.
    4. The largest horizontal displacement occurs in the lower part of pit slopes, because the backfilled part is squeezed by both the north slope and the south slope, and it has a lower elastic modulus than the previous orebody.
    5. Both horizontal displacement and its increment in the south slope are much less than that in the north slope, which means the effect of open-pit to underground mining on the north slope is more prominent and the south slope is more stable.

### 3.3.2 Stress Analysis

Stress analysis is also very important to analyze deformation characteristics, because the north slope and the south slope are influenced by both open-pit

**Fig. 6** Horizontal displacement curves at displacement monitoring points. **a**  $x = 400$ , **b**  $x = 600$ , **c**  $x = 700$



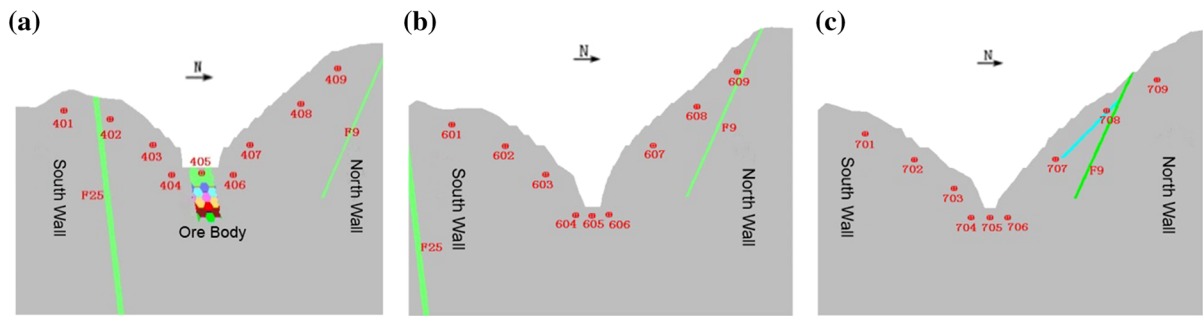


**Fig. 7** Stress monitoring points. **a**  $x = 400$ , **b**  $x = 600$ , **c**  $x = 700$

mining and underground mining and their stress fields will redistribute. Stress concentration may occur somewhere, which may cause the local or overall instability of slopes. Because of the free slope surfaces, stress monitoring points were placed below the surface. Nine stress monitoring points are placed on each section. Stress monitoring points on each cross-section plane were shown in Fig. 7.

Figures 8 and 9 show the maximum and minimum principal stress curves with mining step on different sections, respectively. The distance between slope surface and each stress monitoring point is almost the same. In sections  $x = 400$  and  $x = 600$ , stress variation at the point below the pit floor means the stress variation in backfilling part. The following observations are made:

1. The stress and its variability near the foot of the north slope and the south slope are much larger than other places, indicating that slope foot is most affected by stress redistribution and stress concentration may occur here.
2. The variability of stress decreases with an increasing horizontal distance between the section and orebody, which indicate that the effect of mining operations decreases with an increasing horizontal distance between the section and orebody.
3. In a single section, the largest stress increment occurs before step 3, which indicates that the beginning of open-pit to underground mining influences the stress field most.
4. The location of stress monitoring point No. 405 is in the backfilled part; the stress increases to a stable value with an increasing mining depth,

because the backfilled part is squeezed harder by both the north slope and the south slope when mining to a deeper level.

5. Stress at the stress monitoring points except those near the slope foot changes little, indicating that the influence of open-pit to underground mining on the stress field of pit slopes is local and decays with an increasing vertical distance the orebody.

## 4 Model Experiment

Because the movement and failure of a slope cannot be reflected in numerical simulations, model experiment is necessary to carry out as a supplement for numerical simulations (Song et al. 2010). For more details about the deformation mechanism, a quasi-three-dimensional scaled model corresponding to the section  $x = 400$  in numerical simulation was built.

### 4.1 Similarity Relation

Taking the similarity constant  $C_L = 1/300$  for geometry and  $C_\gamma = 1/1$  for gravity density as primary similarity constants to carry out the model test, full similarity controlling all physical and mechanical parameters in the scope of elasticity can be realized (Elger et al. 2012). Then the ratios of stress, Young's modulus, cohesion can be derived as  $C_\sigma = C_E = C_C = 300$  and the ratios of strain, Poisson's ratio, frictional angle as  $C_\mu = C_\epsilon = C_\phi = 1$ . Based on the similarity constant  $C_L = 1/300$  for geometry, a quasi-three-dimensional scaled model measuring 2400 mm wide by 1450 mm high by 200 mm thick was built.



**Fig. 8** Maximum principal stress curves with mining step. **a**  $x = 400$ , **b**  $x = 600$ , **c**  $x = 700$

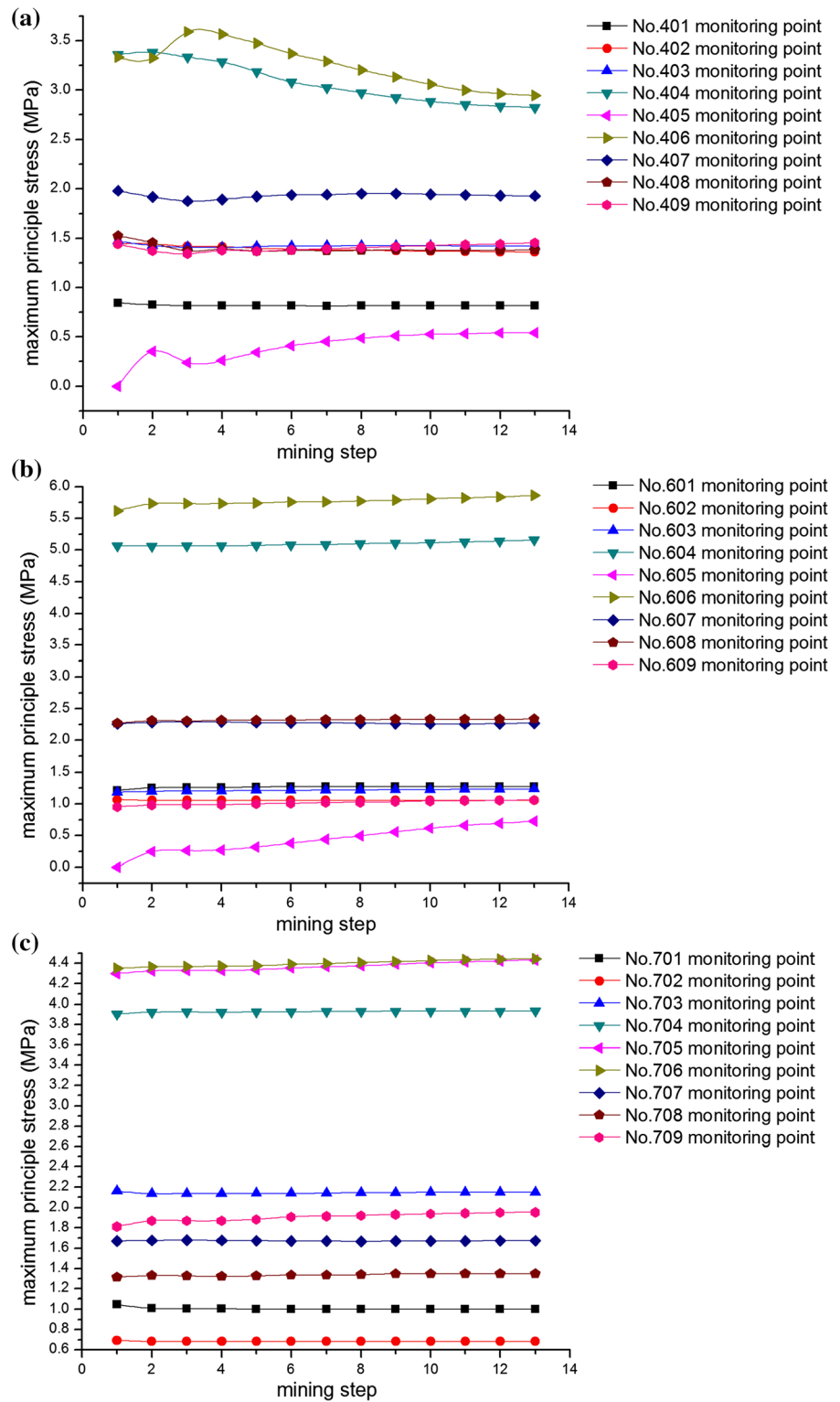


**Fig. 9** Minimum principal stress curves with mining step. **a**  $x = 400$ , **b**  $x = 600$ , **c**  $x = 700$

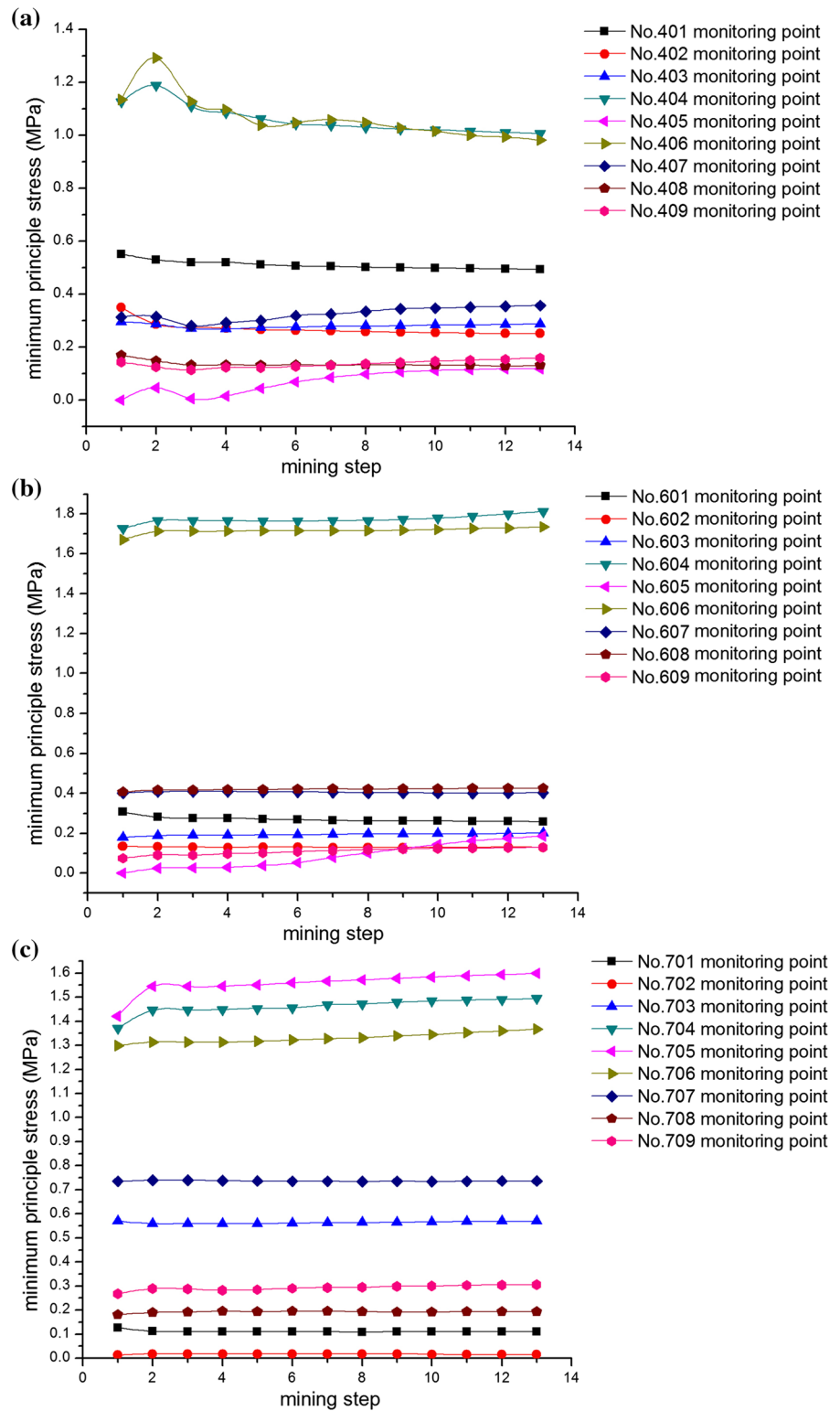


**Table 2** Mix proportion of similar materials

Name	Weight ratio					Weight percentage		
	Barite powder	Iron fine	Quartz sand	Gypsum	Reduced iron powder	Unsaturated resin (%)	Glycerol (%)	Water (%)
Marble	1	1.5	–	–	–	–	3	7
Diorite	5.57	11.5	5.18	1	–	2	–	8
Magnetite	1.73	–	–	–	10	–	7	5

**Table 3** Rock properties in different zones of the similar materials

Name	Young's modulus E(GPa)	Cohesion (MPa)	Frictional angle (°)	Tensile strength (MPa)
Marble	15.6	0.254	28	0.25
Diorite	16.9	0.261	30	0.10
Magnetite	12.5	0.337	40	0.35
Backfilling material	2.0	0.070	27	0.02
Fault	–	0.128	23	–

## 4.2 Similar Materials

The materials' properties can be obtained referring to the engineering geological investigation data and inverse calculation results. Similar materials for rock mass are mainly composed of barite powder, gypsum, iron fine, reduced iron powder, quartz sand, unsaturated resin, glycerol and water. More details about the mix proportion are shown in Table 2. The similar material for the faults is composed of clay placed between polypropylene films. The mechanical parameters of all similar materials are listed in Table 3.

## 4.3 Construction of the Scale Model

Block masonry was adopted to construct the entire model. The adjacent blocks were bonded together by white emulsion to form the whole model in a model casing.

### 4.3.1 Block Making

In order to guarantee the quality and mechanical property of blocks, two sets of block manufacturing dies to make blocks with different sizes of

200 mm × 200 mm × 200 mm and 200 mm × 100 mm × 150 mm, and a set of block manufacturing equipment (shown in Fig. 10) were manufactured. Block manufacturing die is composed of five bolt-fixed steel plates and a movable upper plate. Block manufacturing equipment is composed of block manufacturing die, lifting jack, hydraulic oil pump and reaction frame.

The procedure of making blocks is as follows:

- Step 1* weight different mixtures according to the mix proportion scheme;
- Step 2* mix the weighted mixtures and stir them uniformly;
- Step 3* fill the die with the stirred mixtures and pound them densely preliminarily;
- Step 4* compact them by using lifting jack to make the block denser;
- Step 5* remove the form 5 min later;
- Step 6* dry the shaped blocks in room temperature for 12 h;
- Step 7* maintain the blocks in a drying oven for 3 days at 35 °C; 237 diorite blocks, 193 marble blocks and 65 magnetite blocks are made in all, as shown in Fig. 11



**Fig. 10** Block manufacturing equipment

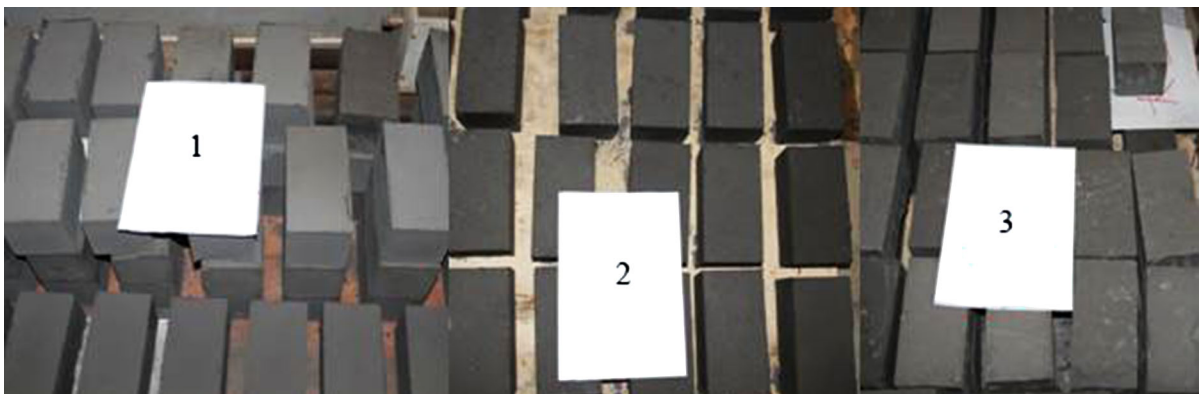


**Fig. 11** Prefabricated blocks (1—diorite blocks, 2—magnetite blocks, 3—marble blocks)

**Table 4** Selected dilutions for similar materials

ID	Block material	White emulsion:water	Cohesion (MPa)	Frictional angle (°)
1	Marble	1:3	0.110	46.5
2	Marble	1:4	0.052	43.3
3	Marble	1:5	0.019	38.2
4*	Marble	1:6	0.023	35.7
5	Marble	1:7	0.008	31.6
6	Diorite	1:3	0.167	49.4
7	Diorite	1:4	0.103	45.9
8*	Diorite	1:5	0.029	42.3
9	Diorite	1:6	0.021	38.5
10	Magnetite	1:3	0.045	48.7
11	Magnetite	1:4	0.012	46.2
12*	Magnetite	1:5	0.018	44.1
13	Magnetite	1:6	0.024	40.6

\* Represents the dilution of white latex is selected for block's bonding

### 4.3.2 Bonding

The quality of the bonding material can significantly affect the success of the overall masonry construction and the following tests. White latex is easy to buy and it has a large bonding strength, so it is diluted with water to control its bonding strength. The shear strength of white latex between the blocks should be exactly equal to the shear strength of blocks, but this objective is impossible to realize. So in order to avoid the sliding of blocks along the interface, the shear strength chosen in this paper is slightly greater than the shear strength of blocks. After a lot of shear tests for white latex of different dilutions, the dilution of white latex for different materials is selected finally. Table 4 lists the shear strength of white latex with different dilutions and the selected dilutions for all the similar materials in this experiment. When constructing the whole model, the diluted white emulsion was evenly spread three times over the contact surfaces ensuring the bond strength.

### 4.4 Monitoring System

The accurate recording of these data as a function of the applied settlement is essential to understand the model behavior and to allow for further validation. Different monitoring techniques were applied to monitor the model response in terms of stresses, displacements and deformations.

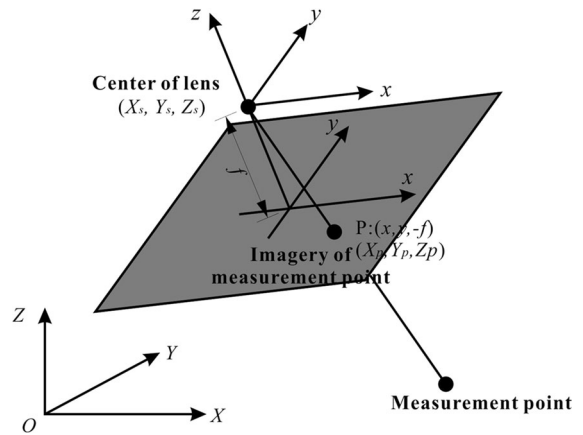


**Fig. 12** Concept of central projection

### 4.4.1 Close-Range Photogrammetry

For a plane strain model test, it was impossible to install a displacement meter on the surface of the model and to carry out direct measurements of the entire rock. A method of non-contact close-range photogrammetry recommended by Wang et al. (2010) was used to measure the movement and deformation of the entire model. This is a technique using photographs, where image and photogrammetric processing take place in order to obtain the shape, size and state of motion.

In this paper, two coordinate systems are assumed: the image coordinate system  $x-y$ , a right-handed  $x-y$

coordinate system which originates at the center of the lens, and the ground coordinate system  $X$ – $Y$ – $Z$ . The coordinate of the monitoring points in the ground coordinate system is denoted by  $(X, Y, Z)$ . The coordinate of the image of monitoring points in the image coordinate system is denoted by  $(x, y, -f)$ , as shown in Fig. 12. Assuming that when the  $y, x$  and  $z$  axes are rotated sequentially in the right screw direction by  $\omega, \phi$  and  $\kappa$ , the rotation matrix from the image coordinate system to the ground coordinate is given by:

$$R = \begin{bmatrix} 1 & 0 & 0 \\ 0 & \cos \omega & -\sin \omega \\ 0 & \sin \omega & \cos \omega \end{bmatrix} \begin{bmatrix} \cos \phi & 0 & \sin \phi \\ 0 & 1 & 0 \\ -\sin \phi & 0 & \cos \phi \end{bmatrix} \begin{bmatrix} \cos \kappa & -\sin \kappa & 0 \\ \sin \kappa & \cos \kappa & 0 \\ 0 & 0 & 1 \end{bmatrix} \quad (1)$$

Representing the elements of the rotation matrix by  $m_{ij}$ , the coordinate of the image of monitoring point can be represented as:

$$\left. \begin{aligned} x &= -f \frac{m_{11}(X - X_s) + m_{12}(Y - Y_s) + m_{13}(Z - Z_s)}{m_{31}(X - X_s) + m_{32}(Y - Y_s) + m_{33}(Z - Z_s)} \\ y &= -f \frac{m_{21}(X - X_s) + m_{22}(Y - Y_s) + m_{23}(Z - Z_s)}{m_{31}(X - X_s) + m_{32}(Y - Y_s) + m_{33}(Z - Z_s)} \end{aligned} \right\} \quad (2)$$

where  $f$  is the distance between the center of lens and the image plane.

In the experiment, drawing grid lines with a horizontal spacing of 10 cm and a vertical spacing of 4 cm on the surface of the model (shown in Fig. 13) and regarding the marked intersection points as measuring points, we could obtain the deformation

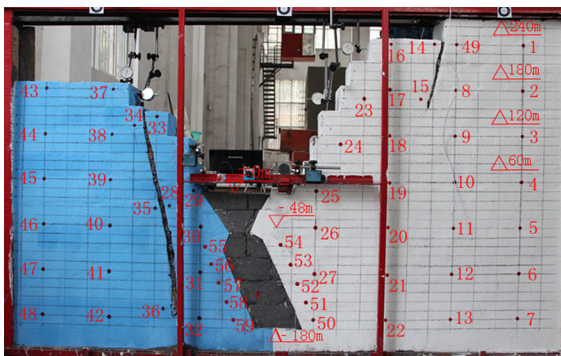


Fig. 13 Monitoring points for digital photogrammetry

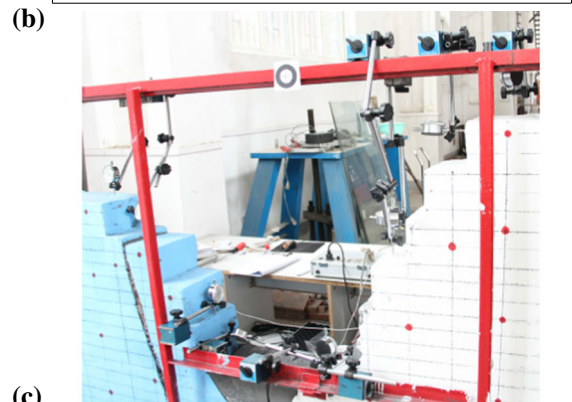
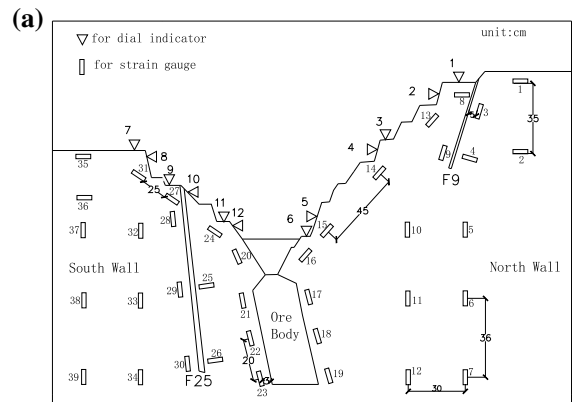


Fig. 14 Arrange of stress and strain monitoring points

of the entire model by comparing the movement of measuring points. If we take two photographs, one before and the second after the experiment, we can obtain the movement of the marked monitoring points in the image coordinate system by comparing the two photographs. Then we can calculate the movement of the marked monitoring points in the ground coordinate system by Eq. (2) and the corresponding moving track shows up.

#### 4.4.2 Dial Indicators

Dial indicators were adopted to measure the vertical and horizontal displacements at the monitoring points on slope surface. The relation between the measured displacements gave an indication of the global response of the slope. In this experiment, 12 dial indicators were installed on the model surface, as shown in Fig. 14.

#### 4.4.3 Stress–Strain Monitoring System

DH-3815N static strain testing system was used to measure the stress and strain, which includes a DH-3815N data logger, a personal computer and the matched “DH-3815N” software. Strain gauges were placed on the model surface. The strain gauges were plotted on the front view, as shown in Fig. 14. All the strain gauges were connected to a DH-3815N data logger. The matched “DH-3815N” software on a personal computer was used to monitor the real-time data collection. If the strain value is measured by sensors, the stress can be easily calculated according to the following equation:

$$\sigma = E\varepsilon \tag{3}$$

where  $\sigma$  is stress at the location of a sensor,  $E$  is the elastic modulus of materials of the physical model, and  $\varepsilon$  is the strain value is measured by sensors.

In this experiment, 39 strain gauges were glued to the model surface.

### 4.5 Results and Discussion

#### 4.5.1 Global Deformation Analysis

Figure 15a shows the displacement vectors when mining down to  $-48$  m, and Fig. 15b shows the displacement vectors when mining down to  $-180$  m. The following observations are made:

1. The deformation nearby the surface of the slopes is large, and displacement vectors are parallel with the surface and point to the pit floor.
2. Displacement vectors nearby the foot of the slopes are inclined upward to the open mine-out area.
3. The effect of open-pit to underground mining on the faults is not prominent.
4. Deformation is dominated by vertical displacement and decreases from up to down; larger horizontal displacement occurs near the foot of slopes.

#### 4.5.2 Subsidence Analysis

Figure 16 shows the total vertical subsidence on different locations when mining down to different levels. The following observations are made:

1. The maximum rebound (25.5 mm) occurs at the foot of the slopes when the open-pit mining ends;
2. The rebound around the foot area decreases gradually from step 2 to step 3, the displacement

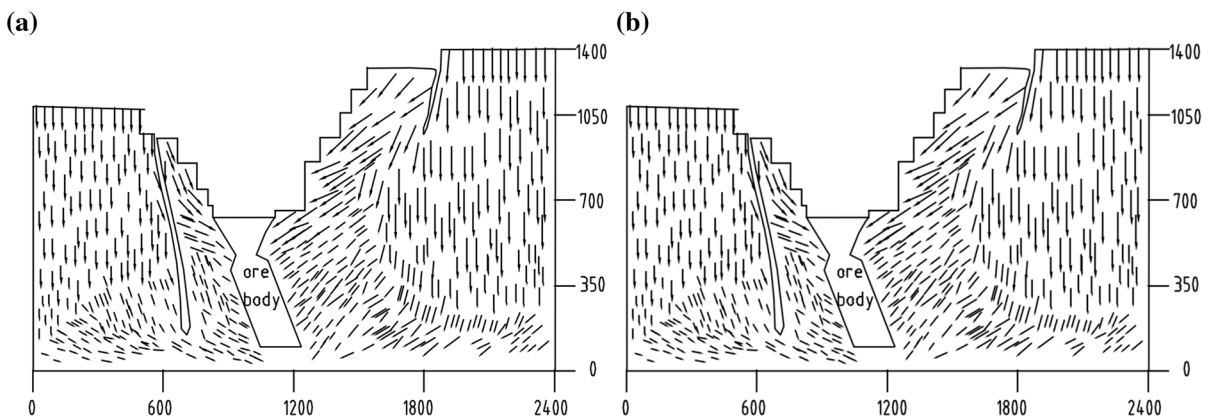


**Fig. 15** Diagram of displacement vectors (unit: mm). **a** mining down to  $-48$  m, **b** mining down to  $-180$  m

**Fig. 16** Subsidence curves with mining step

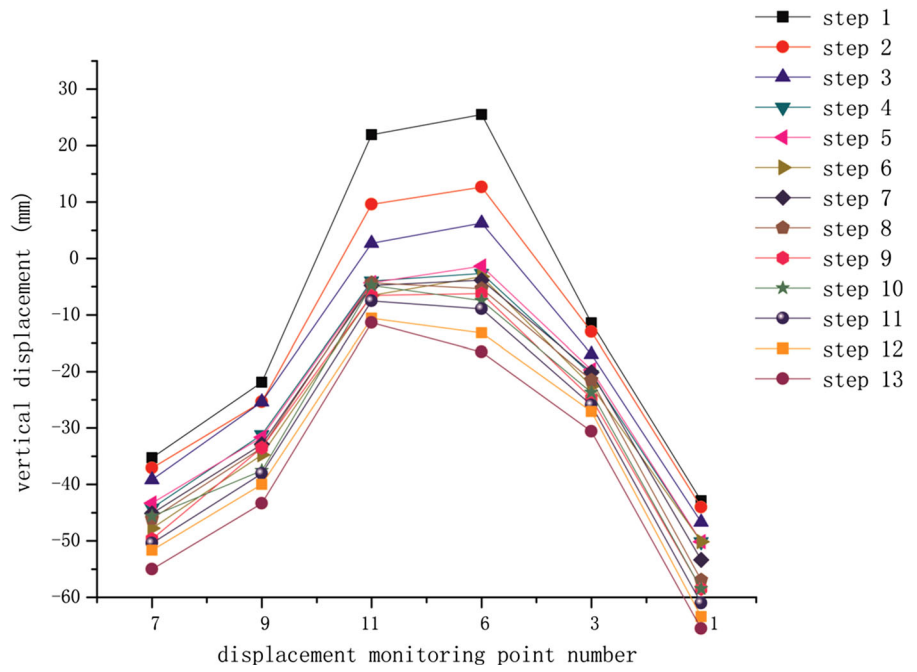
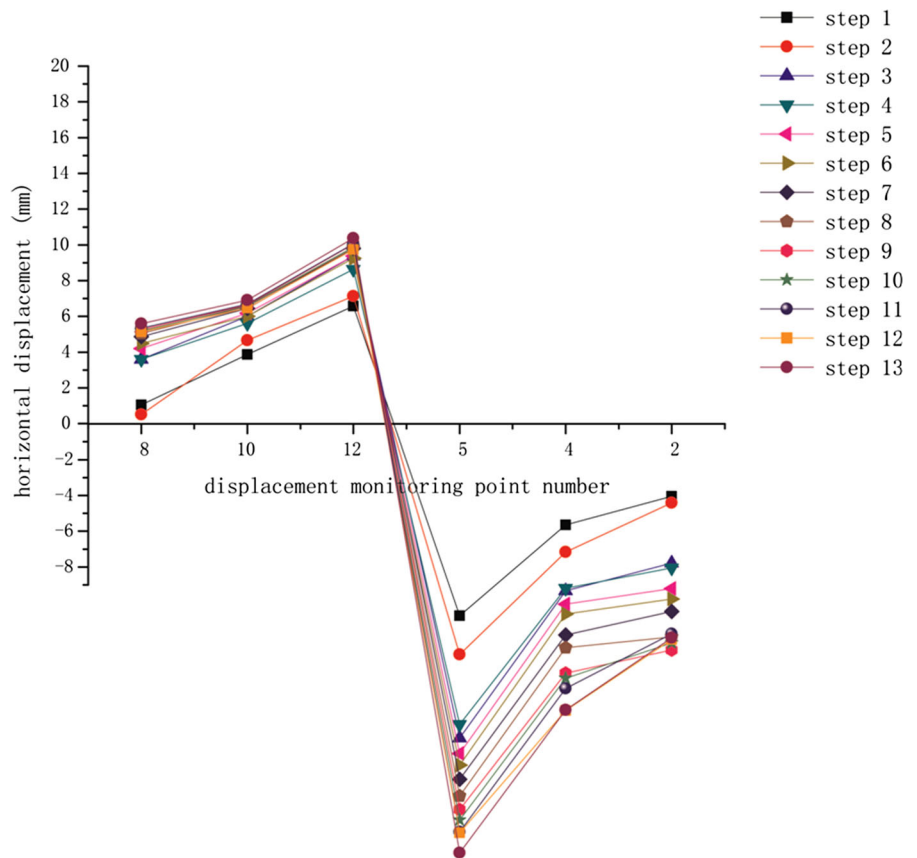


**Fig. 17** Horizontal displacement curves with mining step





at monitoring points of the slopes increases gradually with an increasing mining depth after step 4, the maximum subsidence (about 42 mm) occurs on the crest of the north slope.

3. Subsidence curves are U-shaped.

#### 4.5.3 Horizontal Displacement Analysis

Figure 17 shows the total horizontal displacement on different locations when mining down to different levels. The following observations are made:

1. The displacements at displacement monitoring points increase gradually with an increasing mining depth.
2. The horizontal displacements are in inverse proportion to the increasing relative level;
3. The maximum horizontal displacements of the south and northern slopes, occurring at the foot of the slope, are 27 and 64 mm respectively;
4. The S-shaped deformation curves indicate that open-pit to underground mining affects the stability of the north slope more than the south slope.

#### 4.5.4 Stress Analysis

Figure 18 shows the stress variation at different monitoring points versus mining step. The following observations are made:

Stress at point 15, point 16, point 20 and point 24 (around the toe) is obviously larger than that in other areas.

From step 1 to step 3, Stress at point 16 and point 20 increases from 13.78 to 15.78 kPa and from 13.96 to 14.63 kPa, respectively.

From step 4 to step 13, Stress at point 16 and point 20 decreases to its initial value, which indicates that stress concentration won't have a great effect on the slope stability.

The maximum principle stress at other points does not vary too much during the whole mining process, which indicates that the influence of open-pit to underground mining is quite local.

### 5 Comparison Analysis

#### 5.1 Comparison Between Model Tests and Numerical Simulations

Figures 19, 20 and 21 show the model tested and numerically simulated subsidence at displacement monitoring point 1, horizontal displacement at displacement monitoring point 6 and the maximum principle stress at stress monitoring point 2.

The maximum relative error is 14.9 %. Although there is a significant difference between the results obtained in model tests and numerical simulations, their variation trend is approximately similar.

**Fig. 18** Maximum principle stress curves with mining step

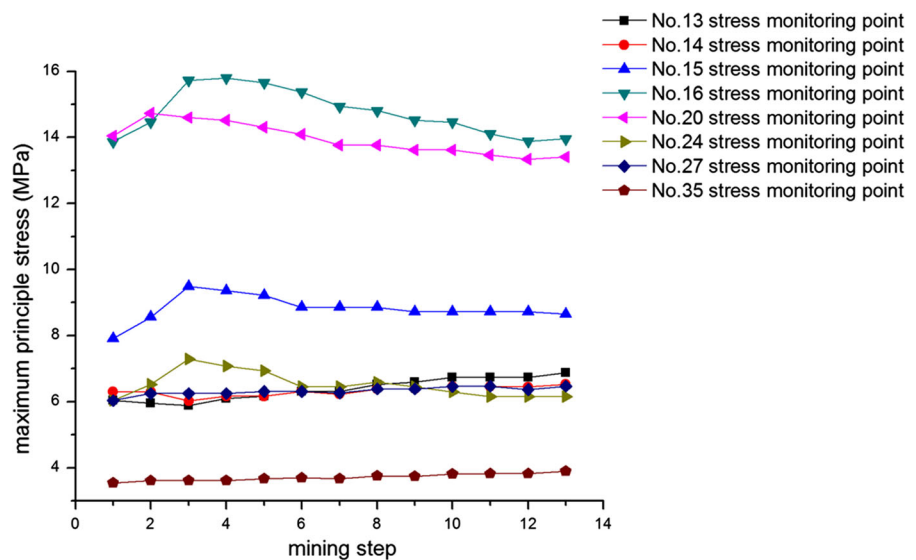


**Fig. 19** Subsidence curves from numerical simulation and model test

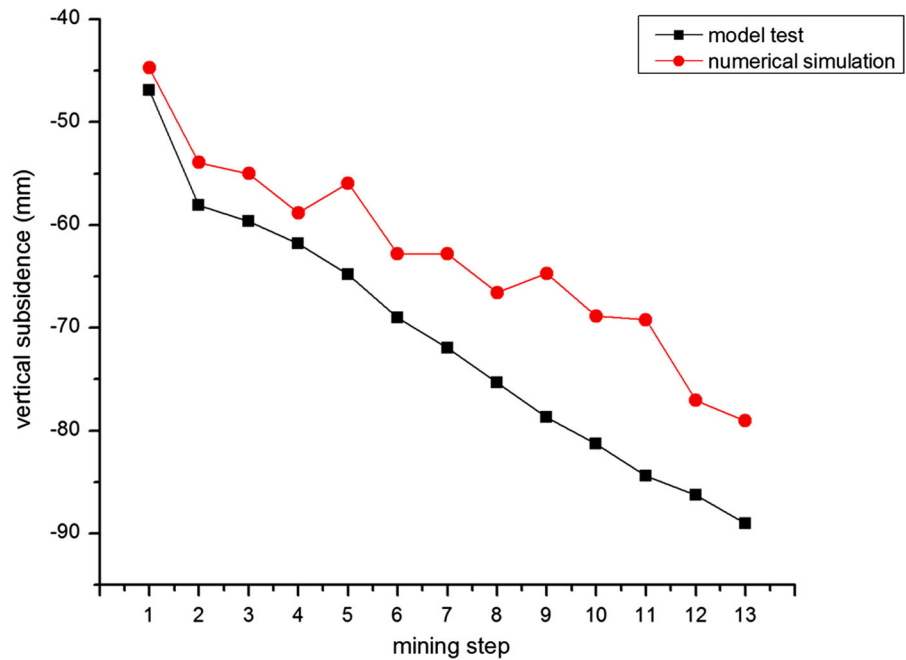
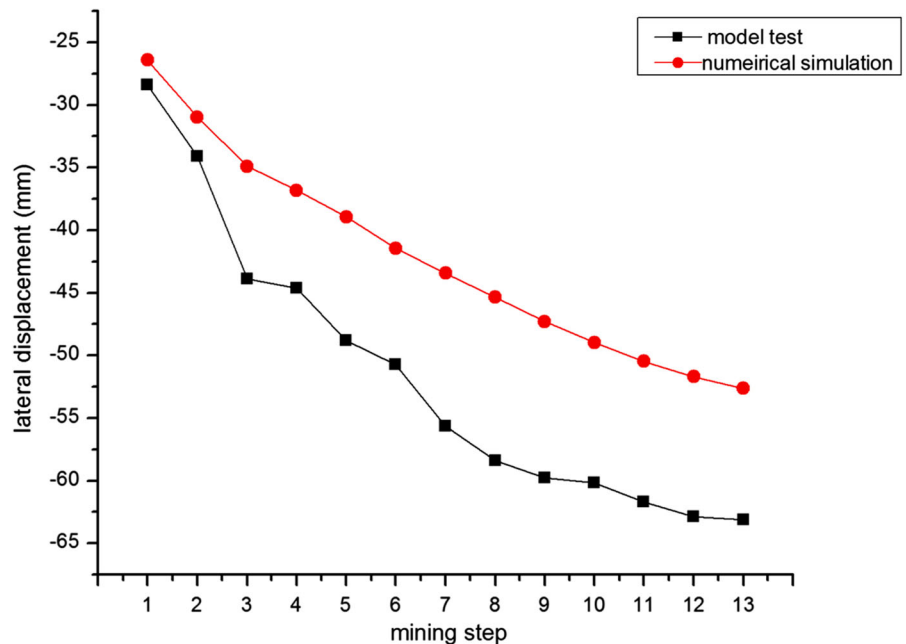


**Fig. 20** Horizontal displacement curves from numerical simulation and model test



## 5.2 Comparison Between Field Tests and Numerical Simulations

Numerical simulations must be verified by field test monitoring data. According to the correlated research achievements (Cai et al. 2005), those deformation monitoring data were extracted for the following analysis.

Monitoring points F9-5 and F9-6 (shown in Fig. 22) are located at +75 m level, F9-5 locates at the instable wedge rock mass and F9-6 locates at the stable slope mass, which are close. Figure 23 shows the field monitoring activities. Both vertical and horizontal displacements are compared with the field monitoring data. The model

**Fig. 21** Maximum principle stresses from numerical simulation and model test

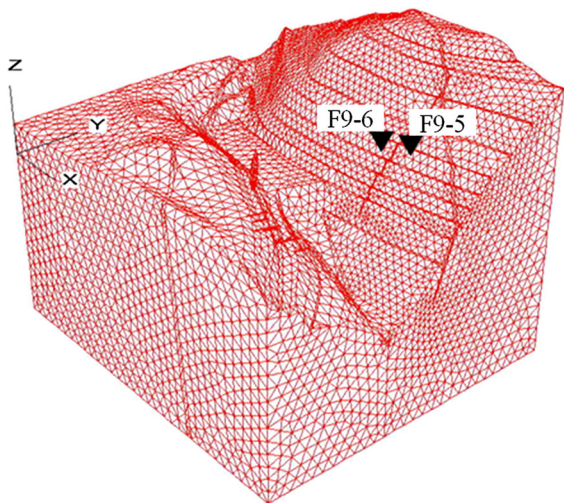
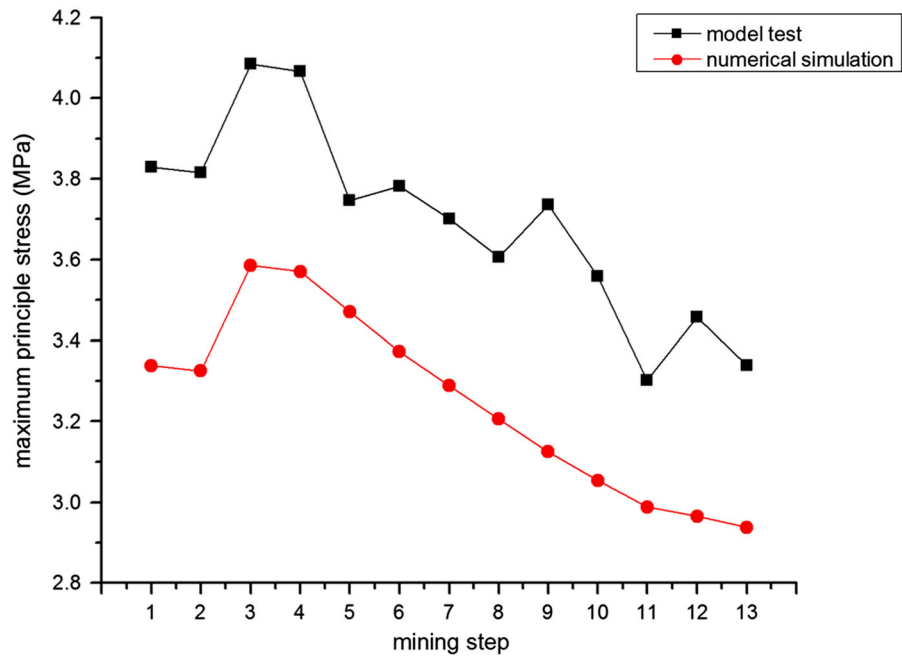


**Fig. 22** Location of monitoring points

tested and numerically simulated displacements are listed in Table 5.

The maximum relative error is as small as 12.5 %, so accuracy requirements can be met to a great extent. Parameters, calculation model and simplified hypothesis are proper and the calculated results are reliable.

The experimental data agree well with the simulated value and the simulated data agree well with the field tested data. The simulation result and model test result have a good reliability.



**Fig. 23** Photo of field monitoring activities

## 6 Conclusions

By analysis of numerical simulation and model test, the following conclusions can be drawn:

1. Numerical simulation and model test are proper to study the deformation of mine slope.
2. Prominent rebound deformation occurs near the foot of slopes because of the unloading induced by open-pit mining. After it is backfilled to 0 m level, the rebound deformation decreases, which

**Table 5** Comparison of the field tested and numerically simulated data

ID	Type	Field test (mm)	Simulation (mm)	Relative error (%)
F9-6	Vertical	35	34.48	1.48
	Horizontal	27	30.38	12.5
F9-5	Vertical	149	143.2	3.89
	Horizontal	112	112.3	0.26

indicate that backfilling mass can restrict the deformation and improve the slope stability.

- Vertical displacement dominates the slope deformation in open-pit to underground mining and it increases with an increasing elevation of monitoring point; the maximum horizontal displacement occurs in the lower part of the slopes, because the backfilled part is squeezed by the north slope and the south slope, and it has a lower elastic modulus than the original orebody. The deformation of south slope is much less than that of the north slope, which implicates that the influence of open-pit to underground mining on slope is proportional to the slope height and the north slope is more likely to destabilize.
- The stress and its variability near the foot of north slope and south slope are much larger than other places, indicating that slope foot is most affected by stress redistribution and stress concentration may occur here; the stress at other stress monitoring points changes little, indicating that the influence of open-pit to underground mining is quite local.
- The effect of open-pit to underground mining on the deformation of the faults is not prominent.
- Mining operations in near ground area affect more on the variation of deformation and stress of pit slopes than that in deeper area.

**Acknowledgments** The study was sponsored by the National Natural Science Foundation of China (Grant Nos. 41372312, 41072219 and 51379194), the Huanghe Yingcai (Science and Technology) program, the Fundamental Research Funds for the Central Universities, China University of Geosciences (Wuhan) (Grant No. CUGL140817) and the China Postdoctoral Science Foundation (Grant No. 2014M552113).

## References

Cai L, Ma J, Zhou Y, Yu J, Ke Q (2005) Deformation monitoring of rocky high slope stability and its application. *Metal Mine* 8:46–48

- Chen S-H, Chen S-F, Shahrour I, Egger P (2001) The feedback analysis of excavated rock slope. *Rock Mech Rock Eng* 34:39–56
- Chen R-H, Kuo KJ, Chen Y-N, Ku C-W (2011) Model tests for studying the failure mechanism of dry granular soil slopes. *Eng Geol* 119:51–63
- Cundall P (1993) *FLAC user's manual*. Itasca Consulting Group, USA
- Daftaribesheli A, Ataei M, Sereshki F (2011) Assessment of rock slope stability using the Fuzzy Slope Mass Rating (FSMR) system. *Appl Soft Comput* 11:4465–4473
- Elger DF, Williams BC, Crowe CT (2012) *Engineering fluid mechanics*. Wiley, Hoboken
- Guo F, Gu W, Tang JJ, Murong MH (2013) Research on deformation stability of soft rock slope under excavation based on FLAC3D. *Appl Mech Mater* 275:290–294
- He L, An X, Ma G, Zhao Z (2013) Development of three-dimensional numerical manifold method for jointed rock slope stability analysis. *Int J Rock Mech Min Sci* 64:22–35
- Huang CZ, Cao YH, Sun WH (2012) Generalized limit equilibrium method for slope stability analysis. *Appl Mech Mater* 170:557–568
- Kaunda RB, Chase RB, Kehew AE, Kaugars K, Selegan JP (2010) Neural network modeling applications in active slope stability problems. *Environ Earth Sci* 60:1545–1558
- Kulatilake P, Wang L, Tang H, Liang Y (2011) Evaluation of rock slope stability for Yujian River dam site by kinematic and block theory analyses. *Comput Geotech* 38:846–860
- Ma Q, Li GJ, Hong Y (2013) The evaluation of stability of rock mass slope based on the block theory and DDA numerical. *Appl Mech Mater* 353:1051–1056
- Song W, Du J, Xingcai Y, Tannant D (2010) Deformation and failure of a high steep slope due to transformation from deep open-pit to underground mining. *J Univ Sci Technol Beijing* 32:145–151
- Tan WH, Li YL, Li CC (2013) Research on 2D limit equilibrium method of slopes considering the effect of horizontal in situ stress. *Adv Mater Res* 671:245–250
- Wang H, Cheng Y, Liang Y, Liang W (2010) Similarity model tests of movement and deformation of coal-rock mass below stopes. *Min Sci Technol (China)* 20:188–192
- Yao X, Reddish D, Whittaker B (1993) Non-linear finite element analysis of surface subsidence arising from inclined seam extraction. *International journal of rock mechanics and mining sciences and geomechanics abstracts*, vol 4. Elsevier, Amsterdam, pp 431–441
- Zhang ZH (2012) Study on the influence mechanism of stability of super high-steep slope in underground mining by caving method. China University of Geosciences, Beijing